

Microscopic origin of liquid viscosity from unstable localized modes

Long-Zhou Huang¹, Bingyu Cui², Vinay Vaibhav³, Matteo Baggioli^{4,*} and Yun-Jiang Wang^{1†}

¹State Key Laboratory of Nonlinear Mechanics, Institute of Mechanics,
Chinese Academy of Sciences, Beijing 100190, China

²School of Science and Engineering, The Chinese University of Hong Kong, Shenzhen, Guangdong, 518172, P. R. China

³Department of Physics “A. Pontremoli,” University of Milan, via Celoria 16, 20133 Milan, Italy

⁴Wilczek Quantum Center, School of Physics and Astronomy,
Shanghai Jiao Tong University, Shanghai 200240, China

Viscosity is the resistance of a liquid to flow, governed by atomic-scale friction between its constituent atoms. While viscosity can be directly computed using the Green-Kubo formalism, its microscopic origin remains poorly understood. In this work, we calculate the viscosity of a $\text{Cu}_{50}\text{Zr}_{50}$ metallic liquid and a Kob-Andersen model in a large range of temperatures and compare the results with a theoretical formula based on nonaffine linear response and instantaneous normal mode theory. This analysis reveals that, above approximately the mode-coupling temperature (T_{MC}), unstable localized instantaneous normal modes (ULINMs) control the viscosity, suggesting a microscopic definition of it as diffusive momentum transport facilitated by local structural excitations mediated by ULINMs as precursors. On the other hand, at $\approx T_{\text{MC}}$, we observe a dynamical crossover below which the viscosity is governed by stable modes. This behavior is compatible with the topological transition that emerges in the potential energy landscape between minima dominated dynamics ($T < T_{\text{MC}}$), corresponding to stable modes, and saddles dominated dynamics ($T > T_{\text{MC}}$), related to unstable ones. Finally, leveraging on the concept of configurational entropy, a quantitative model to connect viscosity with ULINMs is also proposed and validated in both the Arrhenius and non-Arrhenius regimes. In summary, our work provides a microscopic definition of liquid viscosity and highlights the fundamental role of ULINMs as its building blocks, ultimately opening the path to an atomic-scale prediction of viscosity in liquids and glasses.

Introduction– Viscosity is a fundamental transport coefficient in fluid dynamics [1] that reflects the ability of dissipating momentum and determines the resistance to finite rate deformations [2]. In the hydrodynamic regime, viscosity governs the flow of physical systems at very different energy scales, from honey [3] to electrons in ultra-clean metallic systems [4] and ultra-relativistic plasma of quarks and gluons [5].

From a macroscopic point of view, shear viscosity is defined by the linear response relation between shear stress and shear strain rate, that can be formalized using Green-Kubo formalism [6, 7]. This method allows for a direct estimate of the viscosity based on the time correlation function of shear stress, but its application is often hindered by the inevitable presence of hydrodynamic long-time tails [8]. Another established method to compute the viscosity is based on the Einstein-Stokes relation between the self-diffusion constant of a probe particle and the mobility of the fluid in which the latter is flowing [9, 10] (see also [11] for recent developments). However, it is well-known that, as temperature approaches the glass transition, this relation breaks down hindering the applicability of this method.

Moreover, it is important to stress that both the Green-Kubo formula and the Einstein-Stokes relationship do not fully elucidate the microscopic physical mechanisms underlying momentum transport, and ultimately the viscosity itself. In particular, what is the direct link between

microscopic dynamics and macroscopic viscosity in a fluid remains an open question. Using a *hyperbole*, the physical origin of liquid viscosity has not been fully disclosed yet.

In fact, this issue is part of a bigger problem that is the lack of an atomic-scale microscopic description of liquid dynamics and thermodynamics [12, 13], which is mostly due to the absence of a well-defined normal mode formalism for liquids, as achieved on the contrary for crystalline solids [14]. In this context of liquids, the existence of normal modes was already proposed by Zwanzig in 1967 [15], consistent with Maxwell’s intuition [16] that liquids present solid characteristics at short time scales. These ideas were later formalized within the so-called instantaneous normal mode (INM) approach [17, 18], that is based on the diagonalization of the Hessian matrix in instantaneous liquid configurations.

Because of the absence of a well-defined equilibrium configuration in liquids, this procedure inevitably leads to the appearance of negative eigenvalues [19], or equivalently purely imaginary frequencies, that correspond to regions of the potential energy landscape with negative local curvature. Modes corresponding to positive eigenvalues are stable, while those with purely imaginary frequencies are called unstable INMs. The physical meaning of these unstable INMs remains matter of debate, contributing to the famous question of “*what INMs are and are not*” [20].

Partially answering this question, in a series of works [21, 22], Keyes proposed that unstable INMs might provide the fundamental blocks to achieve a microscopic derivation of the liquid self-diffusion constant, highlight-

* b.matteo@sjtu.edu.cn

† yjwang@imech.ac.cn

ing their physical nature as relaxational processes mediated by jumps over potential barriers. It was later clarified that only unstable delocalized INMs contribute to the self-diffusion constant [23, 24] (see also [25–30] for related works and different definitions of this “diffusive” subset of INMs), providing a first connection between microscopic excitations and macroscopic transport in liquids, but leaving the physical meaning of the localized unstable modes unclear.

In this *Letter*, we investigate whether a microscopic definition for another fundamental transport coefficient in liquids – shear viscosity – can be achieved using a normal mode approach. In doing so, we will reveal the so far unknown physical significance of unstable localized modes and their essential role for the microscopic origin of liquid viscosity.

We anticipate that a connection between high-frequency macroscopic elastic moduli and INMs in liquids was already proposed by Stratt [31], alluding to a possible connection between “certain” INMs and liquid viscosity as well. In this *Letter*, we corroborate that such a relation indeed exists and that, above the mode coupling temperature, unstable localized INMs are the building blocks of liquid viscosity. Our results provide a microscopic definition of viscosity, together with a parameter-free prediction for its value as a function of temperature.

Theoretical model and methods – According to the theoretical formalism presented in [32] based on nonaffine viscoelastic response [33], the shear viscosity derived from the imaginary part of the complex shear modulus is given by

$$\eta = 3\rho\tilde{v}(0) \int \frac{g(\omega)\Gamma(\omega)}{m^2\omega^4} d\omega, \quad (1)$$

where $\rho = N/V$ represents the number density, N is the number of atoms and V is the volume of the system. Additionally, $g(\omega)$ is the density of states (DOS); m is the atomic mass; $\Gamma(\omega)$ is the affine force field correlator [33] (see Supplementary Material (SM), Appendix D, for more details); $\tilde{v}(0)$ is the zero-frequency limit of the spectral density, $\tilde{v}(\omega) = \int_0^\infty v(t)e^{-i\omega t} dt$, with $v(t)$ the memory kernel arising from the coupling between tagged particles and thermal environment [34, 35]. All our following results and conclusions will rely on the validity of Eq. (1).

To derive the memory kernel, we use the projection operator formalism [36–38],

$$v(t) = \frac{\langle \mathbf{F}(e^{-i(1-\mathcal{P})\mathcal{L}t}\mathbf{F}) \rangle}{k_B T} = \frac{\langle \mathbf{F}\mathbf{F}_r(t) \rangle}{k_B T} = \frac{\bar{C}_{\mathbf{F}\mathbf{F}}(t)}{k_B T}, \quad (2)$$

where \mathbf{F} is the true force acting on the tagged particle. The random force $\mathbf{F}_r = e^{-i(1-\mathcal{P})\mathcal{L}t}\mathbf{F}$, $-i\mathcal{L}$ is the Liouvillian operator corresponding to the unperturbed dynamics and \mathcal{P} is the Mori projection operator along the direction of the velocity (see SM, Appendix F, for more details). Consequently, the zero-frequency limit of spectral density

can be simply expressed as

$$\tilde{v}(0) = \int_0^\infty \frac{\bar{C}_{\mathbf{F}\mathbf{F}}(t)}{k_B T} dt. \quad (3)$$

Finally, we present two important remarks in applying Eq.(1) to liquid systems. First, the definition of the DOS in liquids is not straightforward. In our work, we will identify $g(\omega)$ with the INM density of states, allowing a direct connection to normal modes (that is not possible using the velocity auto-correlation function). Second, following this choice, it is necessary to define the integration range on ω , that now takes values along both the real and imaginary axes. In the following, in order to find the correct range of integration, we will consider different choices and compare them directly with the simulation data. As already discussed, for the case of the self-diffusion constant [21], only unstable delocalized modes should be considered. It is therefore conceivable that a similar situation will hold for the shear viscosity.

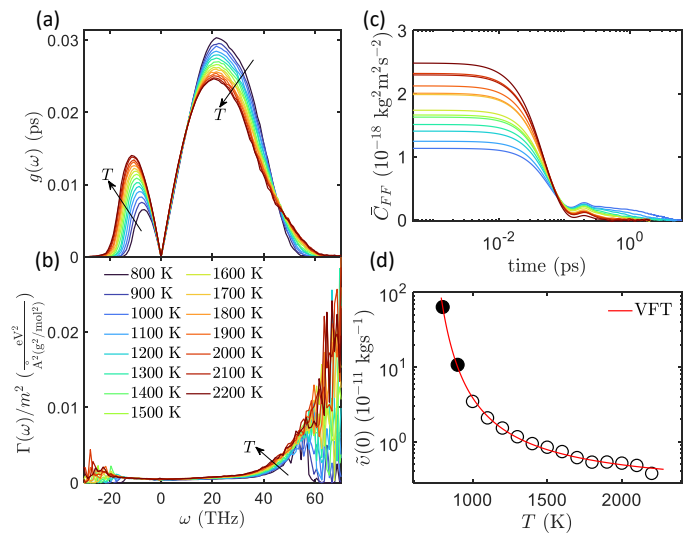


FIG. 1. (a) INM DOS $g(\omega)$ and (b) affine force field correlator $\Gamma(\omega)/m^2$ versus frequency at different temperature. (c) Auto-correlation function of the random force $\bar{C}_{\mathbf{F}\mathbf{F}}(t)$ versus time at different temperature. (d) Temperature dependence of the zero-frequency limit of spectral density $\tilde{v}(0)$. Solid black circles are calculated using Stokes-Einstein relation, while hollow circles by the projection operator technique, Eq. (3).

In this study, two simulation systems are considered: (I) a $\text{Cu}_{50}\text{Zr}_{50}$ metallic liquid with $T_g = 690$ K [39] and (II) a Kob-Andersen (KA) simulation model [40, 41]. Ten independent samples were obtained to reduce the fluctuation error of the simulations. More details about the models and simulations are provided in the SM. The results in the main text refer to the metallic liquid; analogous results for the KA model are presented in the *End Matter* and SM and present the same features showing the universality of microscopic origin of viscosity.

We notice that, once the range of integration on ω in Eq.(1) is fixed, our procedure will not involve any free fitting parameter. Therefore, our results could be taken as a direct test of the validity of Eq.(1) that, to the best of our knowledge, has never been verified.

Microscopic description of liquid dynamics– We performed INM analysis of the $\text{Cu}_{50}\text{Zr}_{50}$ metallic liquid for temperatures between 800 K and 2200 K. The corresponding INM DOS is shown in Fig. 1(a), following the common practice of representing imaginary frequencies along the negative axes [17]. The arrows indicate the directions along which T increases. We notice that $g(\omega)$ is linear at low frequency (see SM, Fig. S3, for more details), in agreement with theoretical expectations (*e.g.*, [21, 42, 43]) and experimental observations [44, 45].

Panels (b) and (c) of Fig. 1 display respectively the re-scaled affine force field versus frequency and the auto-correlation function of the random force versus time at different temperatures. From the memory kernel defined in Eq. (2), we introduce the friction coefficient

$$\gamma = \int_0^{\infty} v(t) dt. \quad (4)$$

We find that computing $\tilde{v}(0)$ using the Einstein's relation $\gamma = k_{\text{B}}T/D$, where D is the long-range diffusion constant of the tagged particles, gives results compatible with those obtained using the projection operator technique, Eq.(3), at low-enough temperatures (see SM, Appendix F). Hence, the Einstein's relation is used only for few data points (solid black circles in Fig. 1(d)) at very low temperatures and, otherwise, $\tilde{v}(0)$ is computed using the projection operator technique. The data also follow the empirical Vogel–Fulcher–Tammann (VFT) equation [46–48], $\eta(T) = \eta_0 \exp\left(\frac{B_{\text{VFT}}}{T-T_0}\right)$, shown with a red line in the same panel.

As anticipated, INMs can be classified into stable and unstable modes depending on the sign of the corresponding eigenvalues. The latter can be further divided into localized and delocalized, depending whether the number of particles participating in the mode is intensive or extensive. Bembenek and Laird originally argued that only unstable delocalized modes are related to diffusion [23, 49], while unstable localized modes do not contribute to it. However, there are indications that unstable localized modes may play a fundamental role for other dynamical properties, such as structural relaxation [50, 51].

In order to quantify the degree of localization, we consider the participation ratio

$$P_{\omega} = \left[N \sum_{i=1}^N (\mathbf{e}_i^{\omega} \cdot \mathbf{e}_i^{\omega})^2 \right]^{-1}, \quad (5)$$

where \mathbf{e}_i^{ω} is the contribution of particle i to the normalized eigenvector corresponding to eigenfrequency ω . P_{ω} takes values between $1/N$ and 1, with the former corresponding to an extremely localized mode with only one

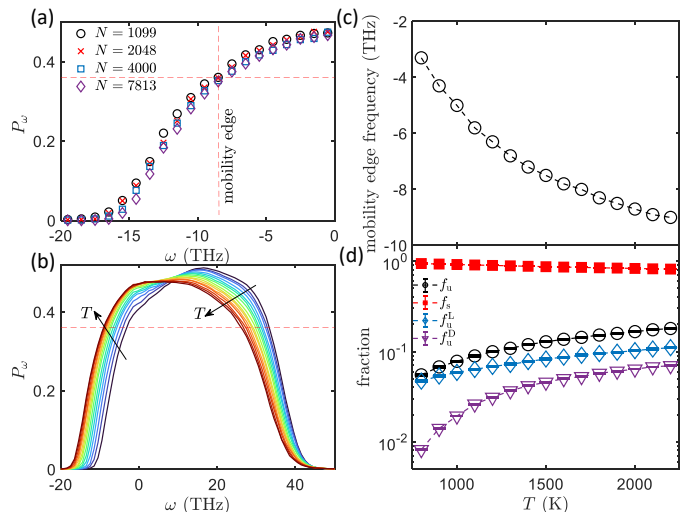


FIG. 2. (a) Variation of the participation ratio as a function of (imaginary) frequency at 1800 K upon changing the size of the simulation box. (b) Participation ratio versus frequency at different temperatures. The dotted horizontal line represents the mobility edge threshold $P_{\omega} = 0.36$. (c) Temperature dependence of the mobility edge frequency. (d) Fraction of stable, unstable, unstable localized and unstable delocalized modes as a function of temperature.

particle participating, while the latter to a fully delocalized mode involving all particles (see SM, Fig. S11, for direct visualization of these two types of modes and Ref. [52] for details about P_{ω}).

In order to identify the *mobility edge* separating localized and delocalized modes, we follow [23, 49] and perform a finite size scaling analysis and compute P_{ω} for different N . In Fig. 2(a), we show P_{ω} as a function of frequency for the unstable branch of INMs and different system sizes. From there, we can observe that P_{ω} becomes system dependent below a certain threshold frequency, that for the CuZr glass-forming system corresponds to $P_{\omega} \approx 0.36$. Intensive modes, with P_{ω} below the mobility edge, are localized, while extensive modes with $P_{\omega} \gtrsim 0.36$ are delocalized.

The participation ratio as a function of frequency for different temperatures is shown in Fig. 2(b). By repeating the same finite size scaling analysis for different T , we found that the value $P_{\omega} \approx 0.36$, defining the mobility edge, is in first approximation independent of temperature (see SM, Fig. S10, for a direct proof of this statement). By then searching for the corresponding (imaginary) frequency (see horizontal dashed line in Fig. 2(b)), we have derived the mobility edge frequency that is plotted in Fig. 2(c) as a function of temperature. We find that the mobility edge frequency increases (in absolute value) by increasing temperature, consistent with the idea that unstable modes tend to be more localized towards the glass transition temperature [23].

Finally, in Fig. 2(d), we respectively show the fraction of stable f_s , unstable f_u , unstable localized f_u^L and unsta-

ble delocalized f_u^D INMs in the temperature range considered. We find that the fraction of stable modes slowly decreases by increasing temperature, while all the other fractions increases with temperature following a similar trend. Once the temperature reaches the glass transition, unstable delocalized modes disappear and all unstable modes become localized, consistent with previous results [24].

We have now independently derived all the physical quantities entering in Eq.(1) and analyzed in detail the different types of modes over which the integration therein could be in principle performed. Before moving to the computation of the liquid viscosity, we notice that, due to the limited size of the simulation box L , the integration in Eq.(1) will be always performed up to a lower cutoff frequency $|\omega_{\min}| = (2\pi v_s)/L$, where the speed of sound v_s is given by $\sqrt{B/\bar{\rho}}$, with B the bulk modulus and $\bar{\rho}$ the mass density (see SM, Appendix H, for more details).

Liquid viscosity— Traditionally, the viscosity can be computed using the Green-Kubo formula [6, 7] (see *End Matter* for a comparison with other methods and experimental data),

$$\eta = \frac{V}{k_B T} \int_0^\infty \langle \sigma_{\alpha\beta}(t) \sigma_{\alpha\beta}(0) \rangle dt, \quad (6)$$

where $\sigma_{\alpha\beta}$ is the α, β component of the stress tensor (with $\alpha, \beta = x, y, x$) and $\langle \dots \rangle$ indicates ensemble average.

In Fig. 3(a), we show the viscosity of the Cu-Zr metallic liquid extracted via Eq. (6) together with the theoretical predictions from Eq. (1) using different sets of normal modes. It emerges clear that using all the instantaneous normal modes in Eq. (1) leads to an incorrect prediction of η by several orders of magnitude, especially at high temperature. Most importantly, we find that the viscosity computed via the Green-Kubo formula is in perfect agreement with the results of Eq.(1) using only ULINMs, and both data are well described by the VFT equation. A closer inspection in the low-temperature regime, provided in Fig. 3(b), reveals the emergence of a dynamical crossover between approximately 800 K and 870 K below which η becomes controlled by the stable modes that correspond to regions of local positive curvature in the potential energy landscape (PEL). This crossover emerges approximately at the mode coupling temperature T_{MC} of the system that is ≈ 840 K and it originates from a topological transition from a dynamics between basins of saddles (“*saddles dominated*”) at $T > T_{MC}$ to a dynamics between basins of minima (“*minima dominated*”) at $T < T_{MC}$ [53, 54]. The observed crossover in η provides a direct manifestation of this topological transition onto the transport properties of the liquid.

Same results are obtained for the Kob-Anderson liquid model and are presented in the *End Matter*, Fig. 6, confirming the excellent agreement found for the CuZr metallic system and the universality of our conclusions.

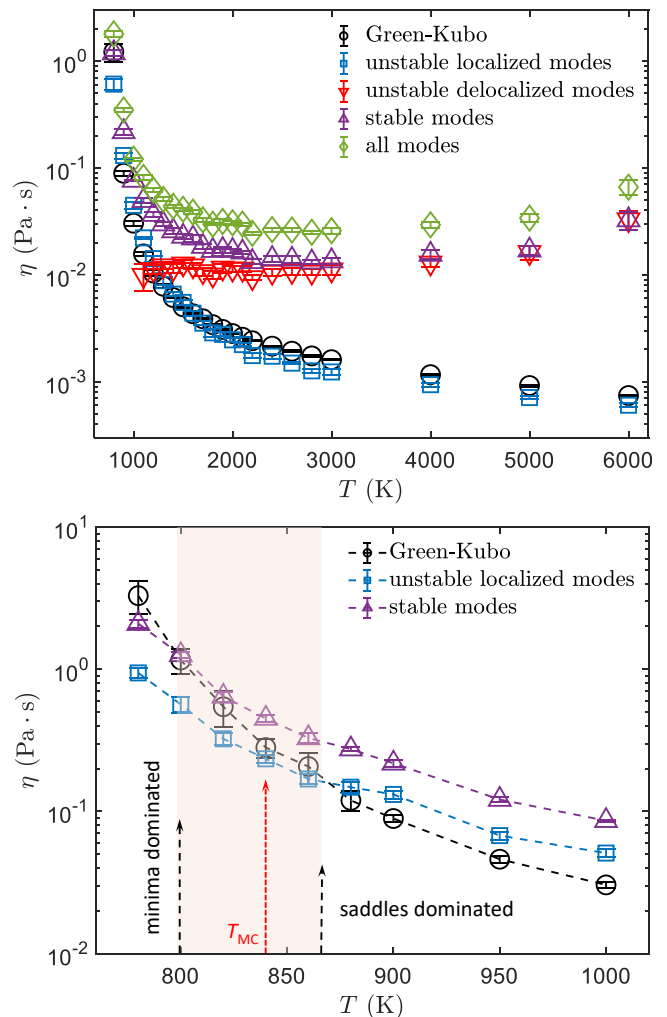


FIG. 3. (a) Comparison of viscosities from Green-Kubo formula (black circles) and different INMs including unstable localized (blue symbols), unstable delocalized (red inverted triangles), stable (purple triangles) and all modes (green diamonds). (b) Zoom on the low-temperature regime. The shaded region defines the dynamical crossover between minima dominated and saddles dominated dynamics. The red arrow locates the approximate position of the mode coupling temperature T_{MC} .

Inspired by Adam-Gibbs theory [55], and motivated by recent results on the relation between liquid diffusion and excess entropy [56], we construct a theoretical model to quantitatively correlate ULINMs with macroscopic viscosity. Following the ideas in [24], we make a similar attempt to link ULINMs to configurational entropy, and then viscosity. First, in Fig. 4(a) we find that the configurational entropy S_{conf} displays a linear relationship with $\ln(f_u^L)$. Here, the configurational entropy is estimated by subtracting the vibrational entropy from the total entropy obtained by thermodynamic integration, as detailed in [57]. Second, we observe that the viscosity follows a direct non-Arrhenius relation with

the configurational entropy, $\eta \propto A \exp\left(\frac{B}{(TS_{\text{conf}})^\lambda}\right)$, with $\lambda = 2.10$. We notice the analogy with the connection between the α relaxation time and S_{conf} , usually rationalized using random first-order transition theory [55, 58, 59]. By combining these two observations, we conclude that $\eta \propto A \exp\left(\frac{B}{(T[a \ln(f_u^L) + b])^\lambda}\right)$, as demonstrated using the simulation data in Fig. 4(c). This result provides a further link between viscosity and ULINMs and validate their intimate relation, providing a bridge between microscopic and macroscopic physics in liquids.

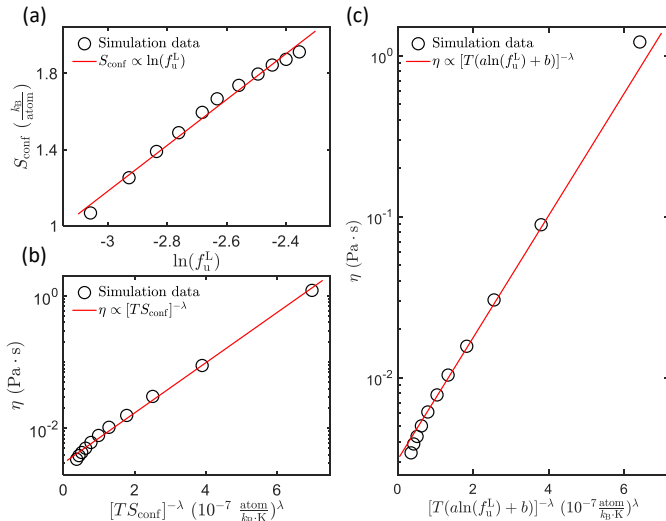


FIG. 4. (a) Linear scaling between S_{conf} and $\ln(f_u^L)$. (b) Viscosity scales as $[TS_{\text{conf}}]^{-\lambda}$, with $\lambda = 2.10$. (c) Viscosity versus $[T(a \ln(f_u^L) + b)]^{-\lambda}$. The solid line indicates the theoretical fit with $a = 1.20$, $b = 4.78$ and $\lambda = 2.10$.

Conclusions— In this *Letter*, we have performed MD simulations combined with instantaneous normal mode analysis to disclose the microscopic origin of viscosity in liquids. Our results indicate that unstable localized INMs are the microscopic excitations responsible for this process. Moreover, our work provides a parameter-free formula to predict from normal modes the viscosity of liquids and its temperature dependence, defying the famous Landau argument that is “*impossible to derive any general formulae giving a quantitative description of the properties of a liquid*” [60].

More in general, our results contribute to answering

the question of what *unstable INMs are and are not*. Unstable delocalized modes are the building blocks for liquid self-diffusion, while the complementary ULINMs are the microscopic facilitators underlying liquid viscosity.

Interestingly, this answer complements several previous analyses. In particular, in Ref.[51] it was shown that localized soft modes are the origin of irreversible structural reorganization. Here, we give a microscopic definition of these localized soft modes and we propose that they should be identified with ULINMs. This is also consistent with the results of [50] that showed that ULINMs act as facilitators of the liquid dynamics, located at the boundary regions between mobile and immobile clusters generated by dynamical heterogeneity. Moreover, our findings are aligned with the idea that, in glass-forming liquid, excitations are localized and relaxation is hierarchical [61]. Finally, viscosity being governed by localized modes is also reflected in the recent results of [62], where it was found that the change in the local barrier energy caused by the fundamental rearrangement or excitation of a *few* particles (hence, localized modes) determines the change in the activation energy and the dynamics of the supercooled liquids.

In summary, it was repeatedly recognized that “*the viscosity of liquids is a subject which has hitherto been without any general theoretical basis*” [63]. By identifying the microscopic carriers of momentum transport, our work suggests a possible microscopic and quantitative theory of liquid viscosity, complementing the previous approaches [1] and providing a new path towards a complete understanding of liquid dynamics.

Acknowledgments – We thank A. Zaccone for collaboration at an early stage of this work and for valuable comments and suggestions. We would like to thank J. Douglas, M. Pica Ciamarra, J. Dyre, T. Keyes, J. Moon, W. Kob and A. Lemaitre for useful comments and discussion. This work was financially supported by the Strategic Priority Research Program (grants nos. XDB0620103 and XDB0510301), the Youth Innovation Promotion Association of Chinese Academy of Sciences, the National Natural Science Foundation of China (grant no. 12072344), and the National Outstanding Youth Science Fund Project (grant No. 12125206). M.B. acknowledges the support of the Shanghai Municipal Science and Technology Major Project (Grant No.2019SHZDZX01) and the sponsorship from the Yangyang Development Fund. B.C. acknowledges supports of the National Natural Science Foundations of China (Grant No.12404232) and the start-up funding from the Chinese University of Hong Kong, Shenzhen (UDF01003468).

- [1] D. S. Viswanath, T. K. Ghosh, D. H. Prasad, N. V. Dutt, and K. Y. Rani, *Viscosity of liquids: theory, estimation, experiment, and data* (Springer Science & Business Media, 2007).
 [2] L. D. Landau and E. M. Lifshitz, *Fluid Mechanics (Sec-*

- ond Edition)* (Pergamon, 1987).
 [3] J. M. Garcia, E. Chambers, Z. Matta, and M. Clark, *Dysphagia* **20**, 325 (2005).
 [4] M. Polini and A. K. Geim, *Phys. Today* **73**, 28 (2020).
 [5] E. Shuryak, *Prog. Part. Nucl. Phys.* **53**, 273 (2004).

- [6] M. S. Green, *J. Chem. Phys.* **22**, 398 (1954).
- [7] R. Kubo, *J. Phys. Soc. Jpn.* **12**, 570 (1957).
- [8] B. J. Alder and T. E. Wainwright, *Phys. Rev. Lett.* **18**, 988 (1967).
- [9] G. G. Stokes, *Mathematical and Physical Papers*, Cambridge Library Collection - Mathematics (Cambridge University Press, 2009).
- [10] T. A. Broadbent, A. B. Einstein, H. Hertz, H. L. Dryden, F. P. Murnaghan, and H. Bateman, *The Mathematical Gazette* **41**, 231 (1928).
- [11] S. G. Moustafa, A. J. Schultz, and J. F. Douglas, *J. Chem. Phys.* **160**, 024114 (2024).
- [12] K. Trachenko, *Theory of liquids: from excitations to thermodynamics* (Cambridge University Press, 2023).
- [13] J. Moon, *Heat Carriers in Liquids: An Introduction* (Springer, 2024).
- [14] J. Moon, L. Lindsay, and T. Egami, *Phys. Rev. E* **108**, 014601 (2023).
- [15] R. Zwanzig, *Phys. Rev.* **156**, 190 (1967).
- [16] J. C. Maxwell, *Phil. Trans. R. Soc.* , 49 (1867).
- [17] T. Keyes, *J. Phys. Chem.* **101**, 2921 (1997).
- [18] T. Keyes, *Normal Mode Analysis: Theory and Applications to Biological and Chemical Systems* (Chapman and Hall/CRC, 2005) Chap. The Relation Between Unstable Instantaneous Normal Modes and Diffusion.
- [19] A. Rahman, M. Mandell, and J. McTague, *J. Chem. Phys.* **64**, 1564 (1976).
- [20] R. M. Stratt, *Acc. Chem. Res.* **28**, 201 (1995).
- [21] T. Keyes, *J. Chem. Phys.* **101**, 5081 (1994).
- [22] T. Keyes, *J. Chem. Phys.* **103**, 9810 (1995).
- [23] S. D. Bembenek and B. B. Laird, *Phys. Rev. Lett.* **74**, 936 (1995).
- [24] V. I. Clapa, T. Kottos, and F. W. Starr, *J. Chem. Phys.* **136**, 144504 (2012).
- [25] J. D. Gezelter, E. Rabani, and B. J. Berne, *J. Chem. Phys.* **107**, 4618 (1997).
- [26] F. Sciortino and P. Tartaglia, *Phys. Rev. Lett.* **78**, 2385 (1997).
- [27] E. La Nave, A. Scala, F. W. Starr, F. Sciortino, and H. E. Stanley, *Phys. Rev. Lett.* **84**, 4605 (2000).
- [28] E. La Nave, A. Scala, F. W. Starr, H. E. Stanley, and F. Sciortino, *Phys. Rev. E* **64**, 036102 (2001).
- [29] J. Chowdhary and T. Keyes, *Phys. Rev. E* **65**, 026125 (2002).
- [30] W.-X. Li and T. Keyes, *J. Chem. Phys.* **107**, 7275 (1997).
- [31] R. Stratt, *Int. J. Thermophys* **18**, 899–907 (1997).
- [32] A. Zaccone, *Phys. Rev. E* **108**, 044101 (2023).
- [33] A. Lemaître and C. Maloney, *J. Stat. Phys.* **123**, 415 (2006).
- [34] B. Cui and A. Zaccone, *Phys. Rev. E* **97**, 060102 (2018).
- [35] B. Cui, J. Yang, J. Qiao, M. Jiang, L. Dai, Y.-J. Wang, and A. Zaccone, *Phys. Rev. B* **96**, 094203 (2017).
- [36] A. Carof, R. Vuilleumier, and B. Rotenberg, *J. Chem. Phys.* **140**, 124103 (2014).
- [37] D. Lesnicki, R. Vuilleumier, A. Carof, and B. Rotenberg, *Phys. Rev. Lett.* **116**, 147804 (2016).
- [38] G. Jung, M. Hanke, and F. Schmid, *J. Chem. Theory Comput.* **13** 6, 2481 (2017).
- [39] M. I. Mendeleev, Y. Sun, F. Zhang, C. Z. Wang, and K. M. Ho, *J. Chem. Phys.* **151**, 214502 (2019).
- [40] W. Kob and H. C. Andersen, *Phys. Rev. E* **51**, 4626 (1995).
- [41] W. Kob and H. C. Andersen, *Phys. Rev. E* **52**, 4134 (1995).
- [42] A. Zaccone and M. Baggioli, *PNAS.* **118**, e2022303118 (2021).
- [43] U. Zürcher and T. Keyes, *Phys. Rev. E* **55**, 6917 (1997).
- [44] C. Stamper, D. Cortie, Z. Yue, X. Wang, and D. Yu, *J. Phys. Chem. Lett.* **13**, 3105 (2022).
- [45] S. Jin, X. Fan, C. Stamper, R. A. Mole, Y. Yu, L. Hong, D. Yu, and M. Baggioli, *Scientific Reports* **14**, 18805 (2024).
- [46] H. Vogel, *Phys. Z* **22**, 645 (1921).
- [47] G. S. Fulcher, *J. Am. Ceram. Soc.* **8**, 339 (1925).
- [48] G. Tammann and W. Hesse, *Z. Anorg. Allg. Chem* **156**, 245 (1926).
- [49] S. D. Bembenek and B. B. Laird, *J. Chem. Phys.* **104**, 5199 (1996).
- [50] W. Zhang, J. F. Douglas, and F. W. Starr, *J. Chem. Phys.* **151**, 184904 (2019).
- [51] A. Widmer-Cooper, H. Perry, P. Harrowell, and D. R. Reichman, *Nat. Phys.* **4**, 711 (2008).
- [52] H. Mizuno and A. Ikeda, in *Low-Temperature Thermal and Vibrational Properties of Disordered Solids: A Half-Century of Universal “Anomalies” of Glasses* (World Scientific, 2023) pp. 375–433.
- [53] L. Angelani, R. Di Leonardo, G. Ruocco, A. Scala, and F. Sciortino, *Phys. Rev. Lett.* **85**, 5356 (2000).
- [54] K. Broderix, K. K. Bhattacharya, A. Cavagna, A. Zippelius, and I. Giardina, *Phys. Rev. Lett.* **85**, 5360 (2000).
- [55] G. Adam and J. H. Gibbs, *J. Chem. Phys.* **43**, 139 (1965).
- [56] I. M. Douglass, J. C. Dyre, and L. Costigliola, *Phys. Rev. Lett.* **133**, 068001 (2024).
- [57] L.-L. Cao and Y.-J. Wang, *J. Phys. Chem. Lett.* **15**, 811 (2024).
- [58] J.-P. Bouchaud and G. Biroli, *J. Chem. Phys.* **121**, 7347 (2004).
- [59] M. Ozawa, C. Scalliet, A. Ninarello, and L. Berthier, *J. Chem. Phys.* **151** (2019).
- [60] L. D. Landau and E. M. Lifshitz, *Statistical Physics: Volume 5*, Vol. 5 (Pergamon, 1980).
- [61] A. S. Keys, L. O. Hedges, J. P. Garrahan, S. C. Glotzer, and D. Chandler, *Phys. Rev. X* **1**, 021013 (2011).
- [62] M. P. Ciamarra, W. Ji, and M. Wyart, *PNAS.* **121**, e2400611121 (2024).
- [63] E. d. C. Andrade, *Nature* **125**, 309 (1930).
- [64] M. Mohr, R. K. Wunderlich, S. Koch, P. K. Galenko, A. K. Gangopadhyay, K. F. Kelton, J.-Z. Jiang, and H.-J. Fecht, *Microgravity. Sci. Tec.* **31**, 177 (2019).
- [65] N. Mauro, M. Blodgett, M. Johnson, A. Vogt, and K. Kelton, *Nat. Commun.* **5**, 4616 (2014).
- [66] S. Nosé, *J. Chem. Phys.* **81**, 511 (1984).
- [67] <https://www.lammmps.org/> .
- [68] R. Hill, *Proc. Phys. Soc. A* **65**, 349 (1952).
- [69] F. Gottwald, S. Karsten, S. D. Ivanov, and O. Kühn, *J. Chem. Phys.* **142**, 244110 (2015).

END MATTER

Appendix A: Extended analysis Cu-Zr metallic liquid - In the main text, we have shown the results for the viscosity η computed using the Green-Kubo formalism, Eq. (6). Alternatively, the viscosity can be obtained from non-equilibrium molecular dynamics using the linear response relation $\eta = \sigma_{\alpha\beta}/\dot{\epsilon}$, where $\dot{\epsilon}$ is the shear strain

rate. We will indicate this second route as *shear MD*. In Fig. 5, we compare the viscosity calculated by different methods: black symbols corresponds to the Green-Kubo formula Eq.(6), red crosses to shear MD and blue symbols are the results obtained from Eq.(1), without free parameters, where the integration is performed over only the unstable localized INMs (ULINMs). For comparison, we also show the experimental data from Refs. [64] (purple diamonds) and [65] (green crosses). At high temperature (above $T \approx 1000$ K, 1.5 times the glass transition temperature), Green-Kubo formula and shear MD are in good agreement. However, when temperature drops, the shear viscosity becomes strain rate dependent and the linear response formula (hence, the shear MD method) is not anymore applicable, giving unreliable predictions for η .

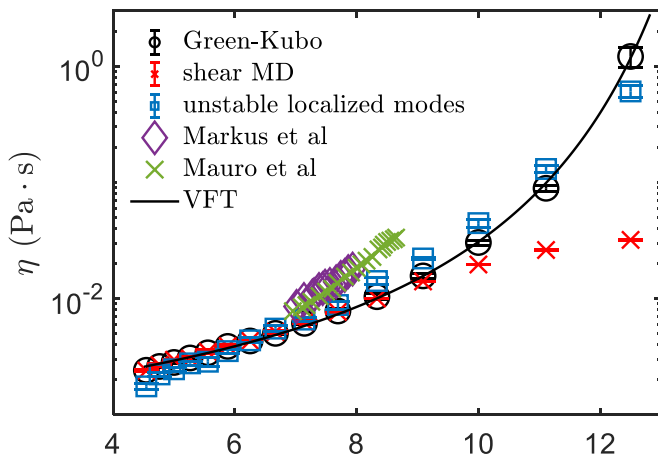


FIG. 5. Comparison of viscosities from the Green-Kubo formula Eq.(6) (black circles), MD non-equilibrium shear (red crosses), the present calculation based on Eq.(1) and unstable localized INMs (blue symbols), and experimental data from Refs. (Markus et al. [64]) (purple diamonds) and (Mauro et al. [65]) (green crosses). The solid line represents the VFT fit.

Appendix B: Viscosity in the KA model - In the main text, we have studied in detail the viscosity of a Cu-Zr metallic liquid and compared the simulation results with the theoretical framework based on instantaneous normal modes. Here, in order to verify the universality and robustness of our findings we present the results of the same analysis for a Kob-Andersen liquid model. More details can be found in SM. In the top panel of Fig. 6, we present the viscosity obtained from the Green-Kubo formalism and we compare it with the predictions from Eq. (1) using unstable localized modes and stable modes.

At high temperature, $T > 0.6$ in LJ units, we find that η is well captured by the theoretical formula using only the ULINMs. In the low temperature region, outlined with a red dashed box, we observe a dynamical crossover below which the viscosity becomes dominated by stable modes rather than unstable localized ones. The bottom panel of Fig. 6 provides a zoom in the low tem-

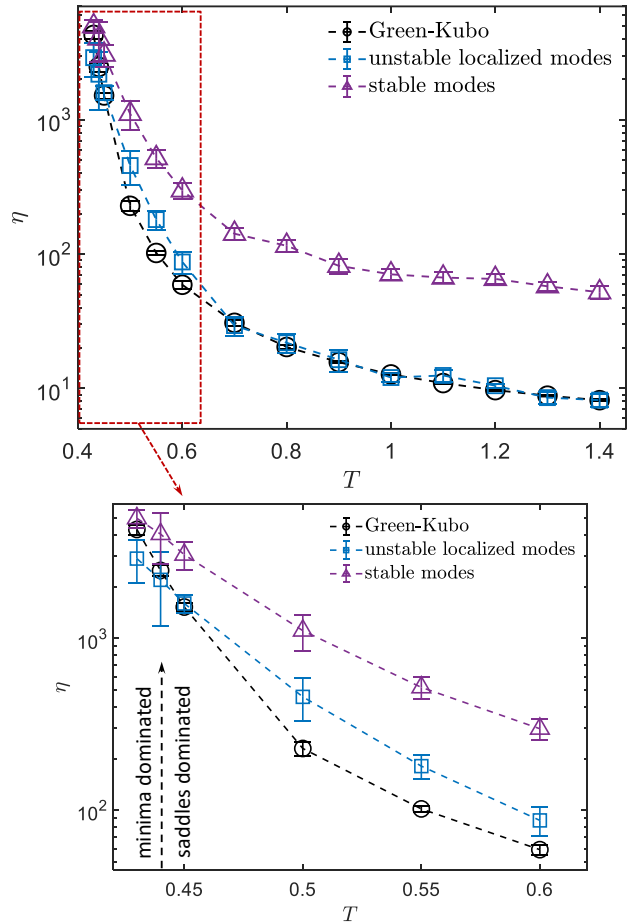


FIG. 6. **Top panel:** Comparison of viscosities for the KA liquid system from the Green-Kubo formula Eq.(6) (black circles) and the theoretical estimates based on Eq.(1) with unstable localized INMs (blue symbols) and stable INMs (purple symbols). **Bottom panel:** A zoom on the low temperature regime indicating the crossover between minima dominated and saddles dominated dynamics that emerges at approximately the mode coupling temperature $T_{MC} \approx 0.44$ (indicated with a vertical dashed arrow).

perature region. We observe that below $T \approx 0.43$ the viscosity from Green-Kubo is governed by stable modes. Interestingly, this scale is compatible with the mode coupling temperature of this system, $T_{MC} \approx 0.44$ confirming that this dynamical crossover in η coincides with the topological transition in the potential energy landscape between minima dominated and saddles dominated dynamics [53, 54].

Supplementary Material

Microscopic origin of liquid viscosity from unstable localized modes

Long-Zhou Huang, Bingyu Cui, Vinay Vaibhav,
Matteo Baggioli, Yun-Jiang Wang

In this Supplementary Material (SM), we provide further details about the numerical and analytical computations presented in the main text. Moreover, we show further analysis on a Kob-Andersen model to corroborate our findings.

Appendix A: Metallic liquid

A semi-empirical potential function is used to simulate the interactions in a $\text{Cu}_{50}\text{Zr}_{50}$ metallic glass with a simulation box of 4000 atoms [39]. The liquid and glass samples are prepared with the standard heating-cooling method. First, a crystalline CuZr phase was heated from 300 K to 2300 K for melting. And then the liquid is thermally equilibrated for 1 ns at 2300 K which is much longer than the α relaxation time. Then the equilibrium liquid was quenched to supercooled liquid to 300 K with constant cooling rate of 10^{10} K/s. The above sample preparation process was carried out under the NPT ensemble with periodic boundary condition. The Nose-Hoover thermostat was used to control temperature and the barostat was used to keep pressure to zero [66]. The kinetic properties were estimated using standard microcanonical (NVE) ensemble after sufficient equilibration at each specific temperature. For statistical purpose, ten independent samples were simulated to reduce the fluctuation of physical quantities. The velocity Verlet algorithm was used to integrate Newton's equations of motion with a time step of 1 fs.

Appendix B: Kob-Andersen model

The Kob-Andersen model is binary Lennard-Jones mixture introduced by Kob and Andersen [40, 41] and defined by the following LJ potential,

$$U_{ab}(r) = 4Y_{ab} \left[\left(\frac{X_{ab}}{r} \right)^{12} - \left(\frac{X_{ab}}{r} \right)^6 \right], \quad (\text{S1})$$

where $a, b \in \{A, B\}$; here $Y_{AA} = 1.0, X_{AA} = 1.0, Y_{AB} = 1.5, X_{AB} = 0.8, Y_{BB} = 0.5,$ and $X_{BB} = 0.88$. The KA model consists of particles A and B with the same mass m in a ratio of 80:20. We use reduced units, where length is in the unit of X_{AA} , temperature Y_{AA}/k_B , and time $(mX_{AA}^2/Y_{AA})^{1/2}$. Under periodic boundary conditions, the system contains 4000 particles. Under the NVT ensemble, the fixed density is 1.185 and the cooling rate is 3.3×10^{-6} . The kinetic properties were calculated using standard microcanonical (NVE) ensemble. Ten independent samples were obtained to reduce the fluctuation error of the simulations. The time step is 0.005. For the KA model, the temperature T will be always displayed in reduced LJ units.

As it can be seen from the Fig. S1(a), the relationship between viscosity and unstable localized mode of Kob-Anderson model is similar to that found in CuZr metallic system, which justifies that the generality of our observation that unstable localized mode are is the physical origin of viscosity in liquid. As shown in Fig. S1(b), the viscosity decreases by increasing the fraction of unstable localized modes. This is consistent with the fact that f_u^L grows with temperature and the viscosity decreases while increasing temperature in the liquid phase.

Appendix C: Instantaneous normal modes

The dynamical matrix for the instantaneous liquid configuration at a given temperature (instantaneous Hessian matrix) is given by

$$\mathbf{D} = \frac{\partial^2 U}{\partial r_{i,\alpha} \partial r_{j,\beta} \sqrt{m_i m_j}}, \quad (\text{S1})$$

where m_i is the mass of particle i and $r_{i,\alpha}$ is the coordinate (x, y or z) of particle i . We directly diagonalize the dynamical matrix and calculate the vibrational density of states as

$$g(\omega) = \lim_{\Delta\omega \rightarrow 0} \frac{\Delta n}{\Delta\omega} = \frac{1}{3N-3} \sum_p \delta(\omega - \omega_p), \quad (\text{S2})$$

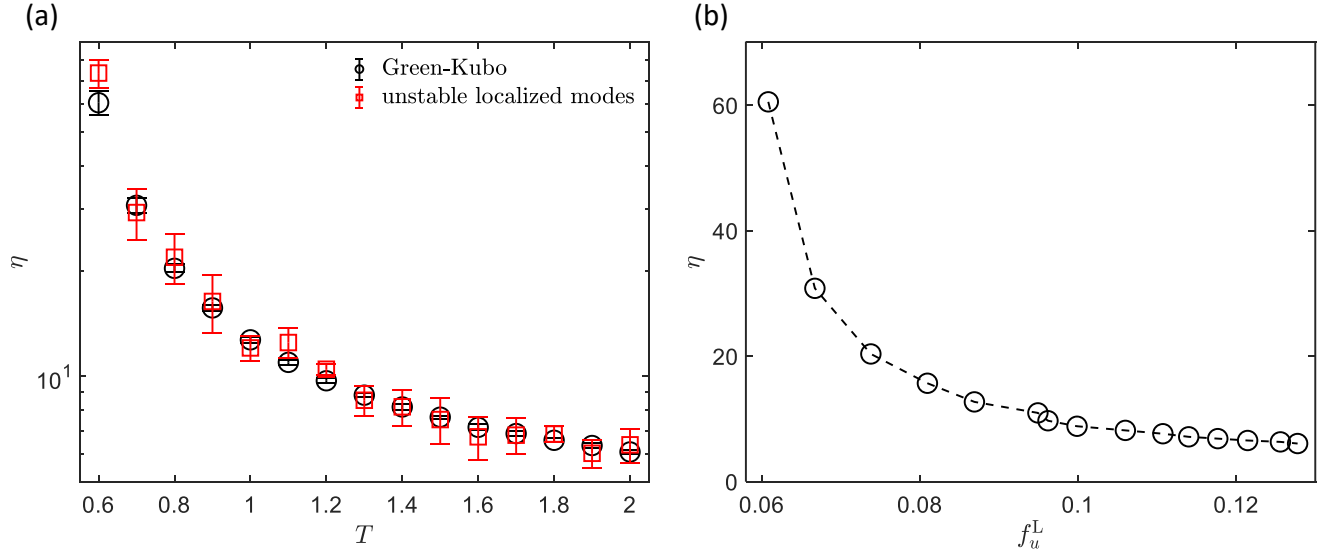


FIG. S1. (a) Comparison of the viscosity of Kob-Anderson model by Green-Kubo approach and Eq. (1) in the main text based on unstable localized modes. (b) Viscosity versus the fraction of unstable localized modes.

where ω_p is the eigenfrequency. Ten independent samples were obtained to reduce the fluctuation error of the simulations.

The results for the INM DOS are shown in Fig. S2 and present similar features as for the metallic liquid discussed in the main text.

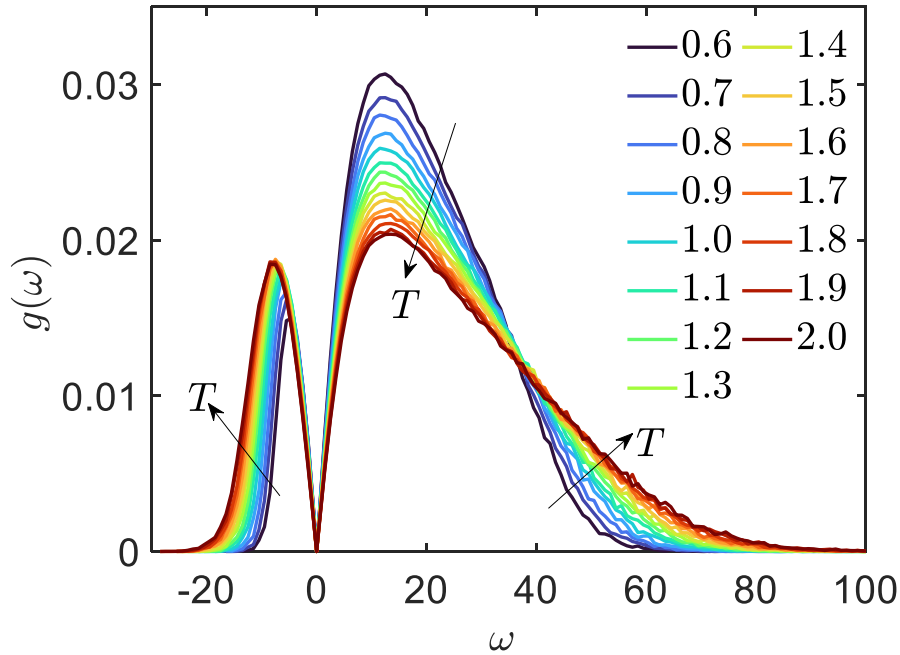


FIG. S2. Instantaneous normal mode DOS for the Kob-Anderson model at different temperature. The arrows indicate the trend of change with increasing temperature.

A zoom of the low frequency region of $g(\omega)$ for the CuZr metallic glass-forming liquid is shown in Fig. S3. The data confirm the linear scaling $g(\omega) = a(T)|\omega|$ (with $a(T)$ growing with temperature) discussed in the main text.

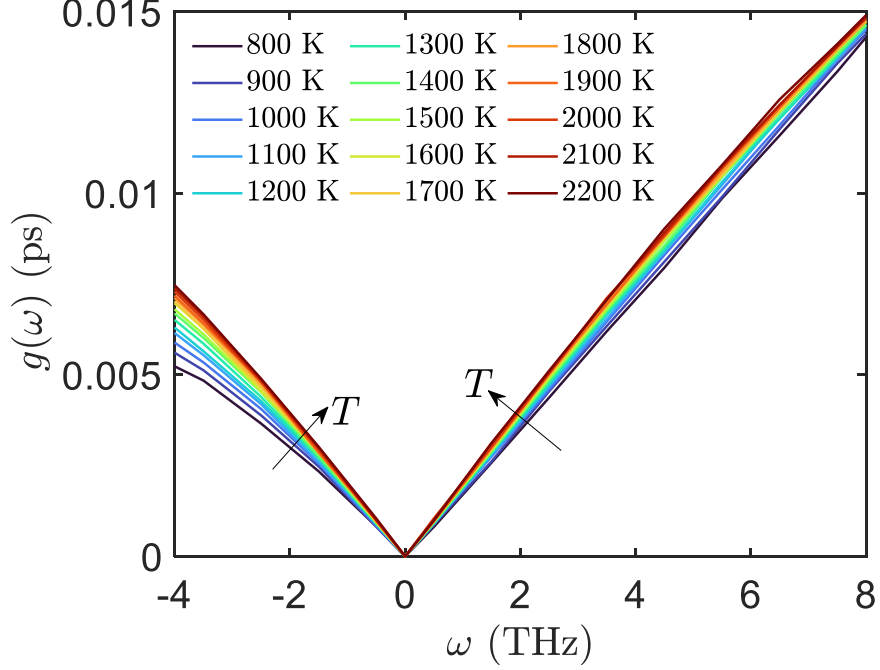


FIG. S3. Zoom of the low frequency region of $g(\omega)$ for the CuZr metallic glass-forming liquid. A linear behavior $g(\omega) = a(T)|\omega|$ emerges at low frequency. From our simulation data, it is also evident that $a(T)$ grows with T .

Appendix D: Affine force field correlator

According to nonaffine lattice dynamics theory [33], the affine force field is obtained from

$$\Xi_{i,xy} = \left. \frac{\partial \mathbf{f}_i}{\partial \varepsilon_{xy}} \right|_{\varepsilon \rightarrow 0} = \frac{\mathbf{f}_i^1 - \mathbf{f}_i^0}{\varepsilon_{xy}}, \quad (\text{S1})$$

where \mathbf{f}_i^1 is the force on the i atom in deformed state; \mathbf{f}_i^0 is the force on the i atom in undeformed state; ε_{xy} is the simple shear strain. The projection of the eigenvectors \mathbf{v}^{ω_p} of the Hessian matrix onto the affine force field are then given by

$$\hat{\Xi}_{p,xy} = \mathbf{v}^{\omega_p} \cdot \Xi_{xy}, \quad (\text{S2})$$

and the affine force field correlator is derived from

$$\Gamma(\omega) = \left\langle \hat{\Xi}_{p,xy}^2 \right\rangle_{\omega_p \in [\omega, \omega + d\omega]}. \quad (\text{S3})$$

A shear strain of 0.0001 is applied in our simulation of Kob-Anderson model and CuZr metallic glass. The affine force field correlator of the Kob-Anderson model is shown as a function of frequency, for the liquid sample at different temperature as shown in the Fig. S4.

Appendix E: Mean square displacement

The diffusion constant can be obtained from the mean square displacement (MSD) as a function of time

$$D_\alpha = \frac{1}{2} \lim_{\tau \rightarrow \infty} \frac{\left\langle [r_{i,\alpha}(t + \tau) - r_{i,\alpha}(t)]^2 \right\rangle}{\tau}. \quad (\text{S1})$$

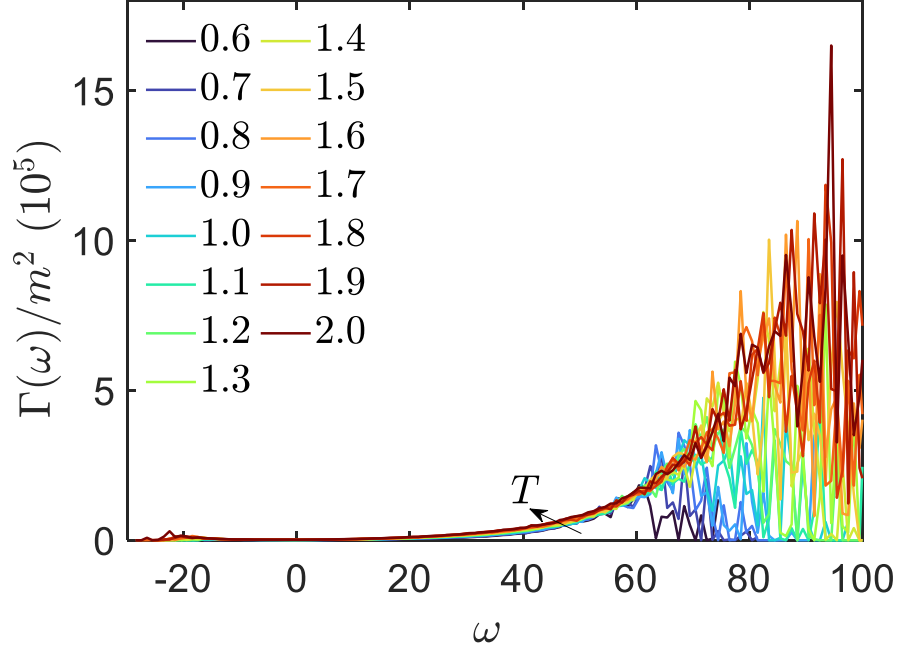


FIG. S4. Affine force field correlator versus frequency at different temperature for the Kob-Anderson model. All the curves are obtained by averaging over 10 independent samples.

The average diffusion constant in an isotropic system in 3D is given by

$$D = \frac{1}{3} \sum_{\alpha=1}^3 D_{\alpha}. \quad (\text{S2})$$

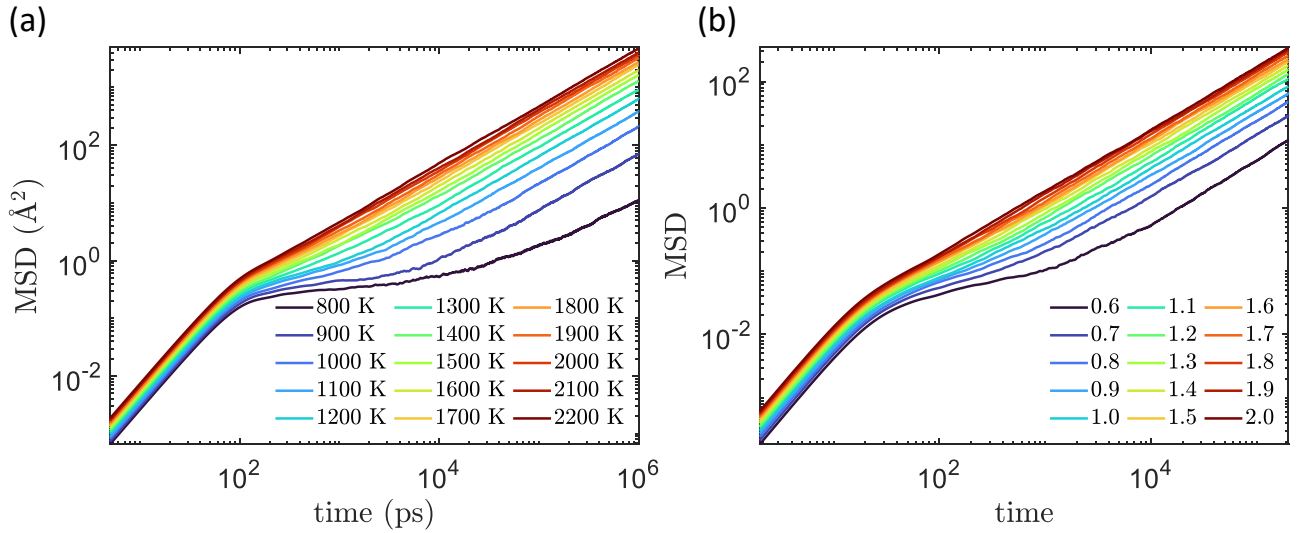


FIG. S5. The mean square displacement as a function of time. (a) CuZr metallic liquid and (b) Kob-Anderson model.

Appendix F: Projection operator technique

According to the projection operator technique [36–38], the memory kernel

$$v(t) = \frac{\langle \mathbf{F} (e^{-i(1-\mathcal{P})\mathcal{L}t} \mathbf{F}) \rangle}{k_B T} = \frac{\langle \mathbf{F} \mathbf{F}_r(t) \rangle}{k_B T} = \frac{\bar{C}_{\mathbf{F}\mathbf{F}}(t)}{k_B T}, \quad (\text{S1})$$

where \mathbf{F} the true force acting on the tagged particle. Based on the second-order backward algorithm, $\bar{C}_{\mathbf{A}\mathbf{A}}(t) = \langle \mathbf{A}_0 \mathbf{A}_t^- \rangle$, where \mathbf{A} is an observable, and $\mathbf{A}_t^- = e^{-i(1-\mathcal{P})\mathcal{L}t} \mathbf{A}_0$. \mathbf{F}_t^- evolves according to the backward orthogonal dynamics

$$\mathbf{F}_{t+\delta t}^-(\mathbf{q}, \mathbf{p}) = \mathbf{F}_t^-(\mathbf{q}^{\delta t}, \mathbf{p}^{\delta t}) + \int_0^{\delta t} \mathbf{F}_{-u}(\mathbf{q}^{\delta t}, \mathbf{p}^{\delta t}) \frac{\langle \mathbf{P}_0 \mathbf{F}_{t-u}^- \rangle}{\langle \mathbf{P}_0^2 \rangle} du, \quad (\text{S2})$$

where \mathbf{q} and \mathbf{p} are respectively the atomic positions and momenta. The second-order propagator

$$F_{n+1}^-(m) = F_n^-(m) + \beta(n) F_n(m) \frac{\delta t}{2} + \frac{F_n(m)}{1 - \frac{\delta t}{2} \kappa(n)} \left[\gamma(n) + \Delta(n) \beta(n) \frac{\delta t}{2} \right] \frac{\delta t}{2}, \quad (\text{S3})$$

with

$$\beta(n) = \frac{\sum_{m=1}^{N_{\text{traj}} - N_{\text{corr}}} P_n(m) F_n^-(m)}{\sum_{m=1}^{N_{\text{traj}} - N_{\text{corr}}} P_n(m)^2} \quad (\text{S4})$$

$$\kappa(n) = \frac{\sum_{m=1}^{N_{\text{traj}} - N_{\text{corr}}} F_n(m) P_n(m)}{\sum_{m=1}^{N_{\text{traj}} - N_{\text{corr}}} P_n(m)^2} \quad (\text{S5})$$

$$\gamma(n) = \frac{\sum_{m=1}^{N_{\text{traj}} - N_{\text{corr}}} P_n(m) F_n^-(m+1)}{\sum_{m=1}^{N_{\text{traj}} - N_{\text{corr}}} P_n(m)^2} \quad (\text{S6})$$

$$\Delta(n) = \frac{\sum_{m=1}^{N_{\text{traj}} - N_{\text{corr}}} F_n(m) P_n(m+1)}{\sum_{m=1}^{N_{\text{traj}} - N_{\text{corr}}} P_n(m)^2}. \quad (\text{S7})$$

As a result, based on the trajectories of the atoms in each configuration we can get \mathbf{F}_t^- . Finally, \bar{C}_{FF} can be obtained,

$$\bar{C}_{FF}(n\delta t) = \frac{1}{N_{\text{traj}} - N_{\text{corr}}} \sum_{m=1}^{N_{\text{traj}} - N_{\text{corr}}} F_n(m) F_n^-(m). \quad (\text{S8})$$

As shown explicitly in Fig. S7, the results for the friction coefficient obtained using $\int_0^\infty \bar{C}_{\mathbf{F}\mathbf{F}}(t)/k_B T dt$ and $k_B T/D$ are in good agreement. Therefore, we will use $k_B T/D$, instead of $\int_0^\infty \bar{C}_{\mathbf{F}\mathbf{F}}(t)/k_B T dt$, to calculate $\bar{v}(0)$ at low temperatures.

Appendix G: Participation ratio

The participation ratio of Kob-Anderson model is calculated and analyzed in Fig. S8 and displays features similar to the case of the CuZr metallic glass-forming liquid discussed in the main text.

As done in the main text, we can calculate the dependence of the mobility edge frequency on temperature for the KA model, as shown in the Fig. S9.

Meanwhile, variation of the participation ratio of CuZr metallic glass-forming liquid as a function of (imaginary frequency) at 1500 K and 2100 K upon changing the size of the simulation box as shown in the Fig. S10. A typical localized and delocalized mode are shown by the magnitude of each particles vibrational vector as shown in the Fig. S11. Several high amplitude eigenvectors at local frequencies indicate strong localization, indicating that the energy associated with these modes is confined to a small spatial region.

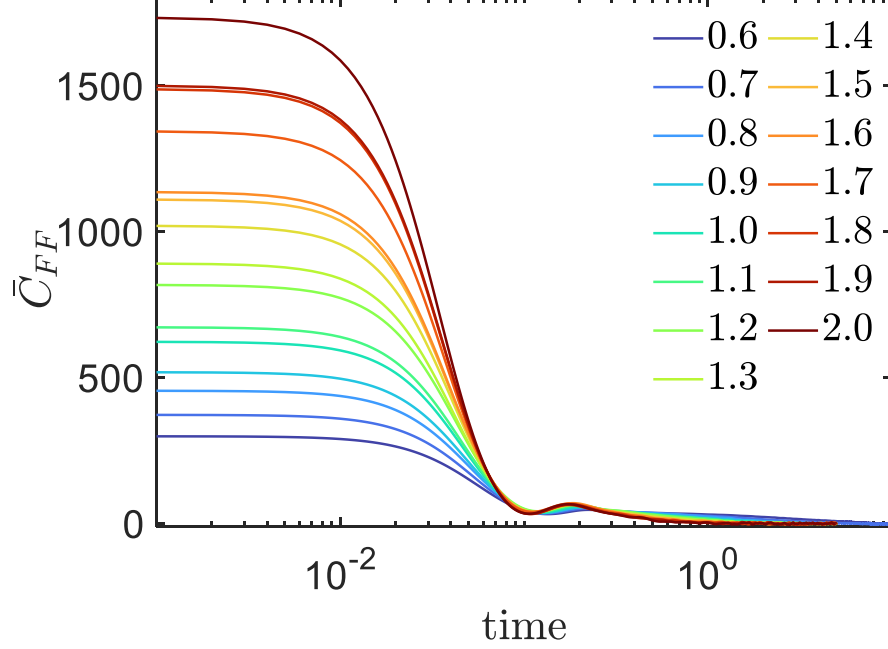


FIG. S6. Auto-correlation function versus time at different temperatures $T \in [0.6, 2]$ for the KA model. LJ units are used for the temperature T .

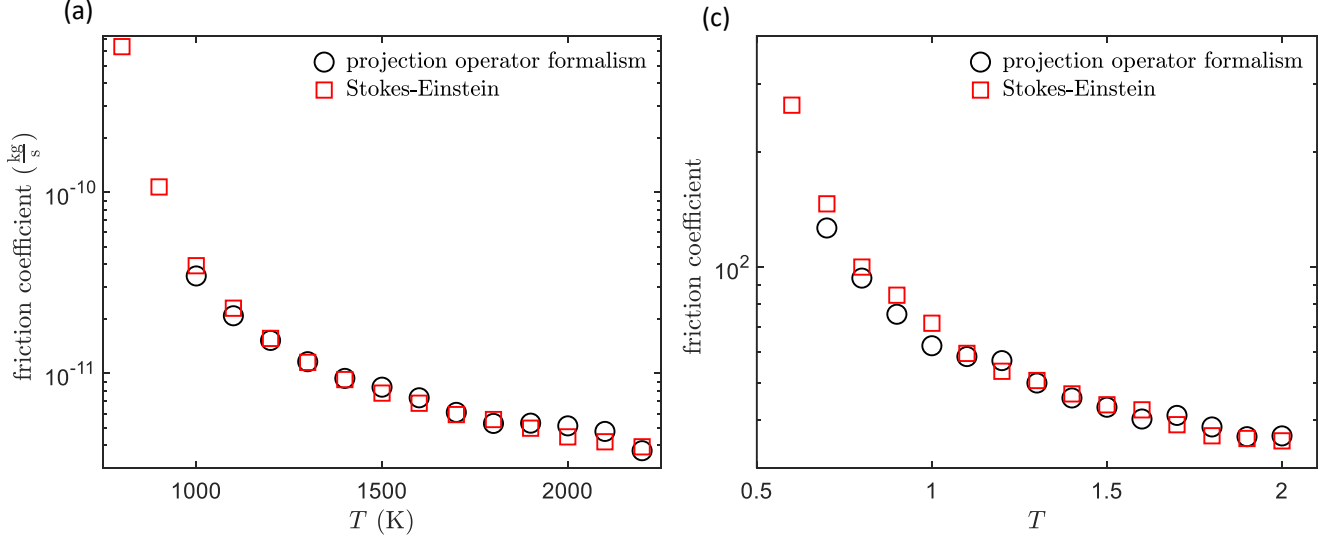


FIG. S7. Consistency of $\int_0^\infty \bar{C}_{\mathbf{FF}}(t)/k_B T dt$ and $k_B T/D$ for calculating the friction coefficient. (a) CuZr glass-forming liquid and (b) Kob-Anderson model.

Appendix H: Bulk modulus

The elastic constants are calculated using LAMMPS [67], and then bulk modulus can be obtained according to the Voigt-Reuss-Hill approximation [68]. In the Fig. S12, it is shown that the bulk modulus of CuZr decreases with increasing temperature. Fig. S13 shows the value of the cutoff frequency, $|\omega_{\min}| = (2\pi\sqrt{B/\bar{\rho}})/L$, as a function of temperature for the CuZr metallic liquid.

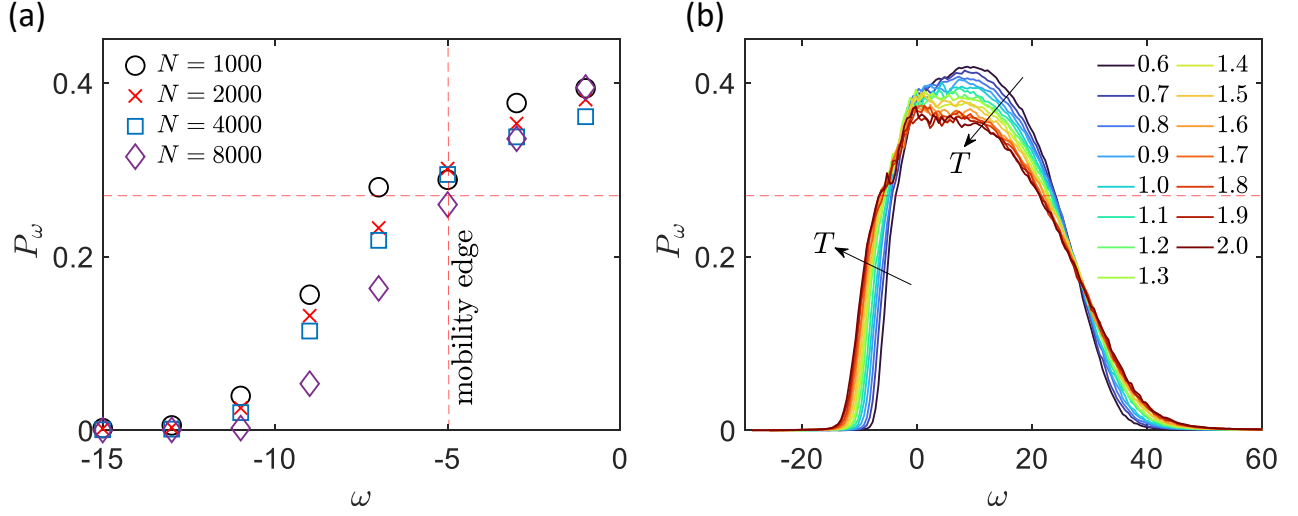


FIG. S8. The participation ratio of Kob-Anderson model. (a) Variation of participation ratio with mode size at temperature 1; (b) Participation ratio versus frequency at different temperature. The dotted horizontal line represents $P_\omega = 0.27$.

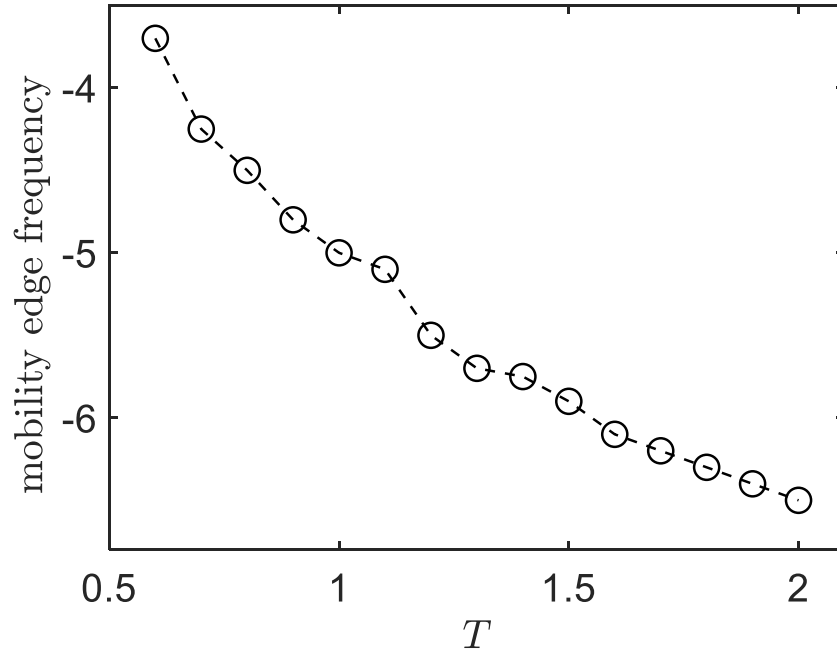


FIG. S9. Temperature dependence of the mobility edge frequency for the Kob-Anderson model.

Appendix I: Vogel-Fulcher-Tammann (VFT) equation

The VFT equation reads [46–48]

$$\eta(T) = \eta_0 \exp\left(\frac{B_{\text{VFT}}}{T - T_0}\right), \quad (\text{S1})$$

where η_0 is the viscosity in the infinite temperature limit, T_0 is the temperature at which the viscosity diverges and B_{VFT} denotes the fragility strength coefficient related with the activation barrier.

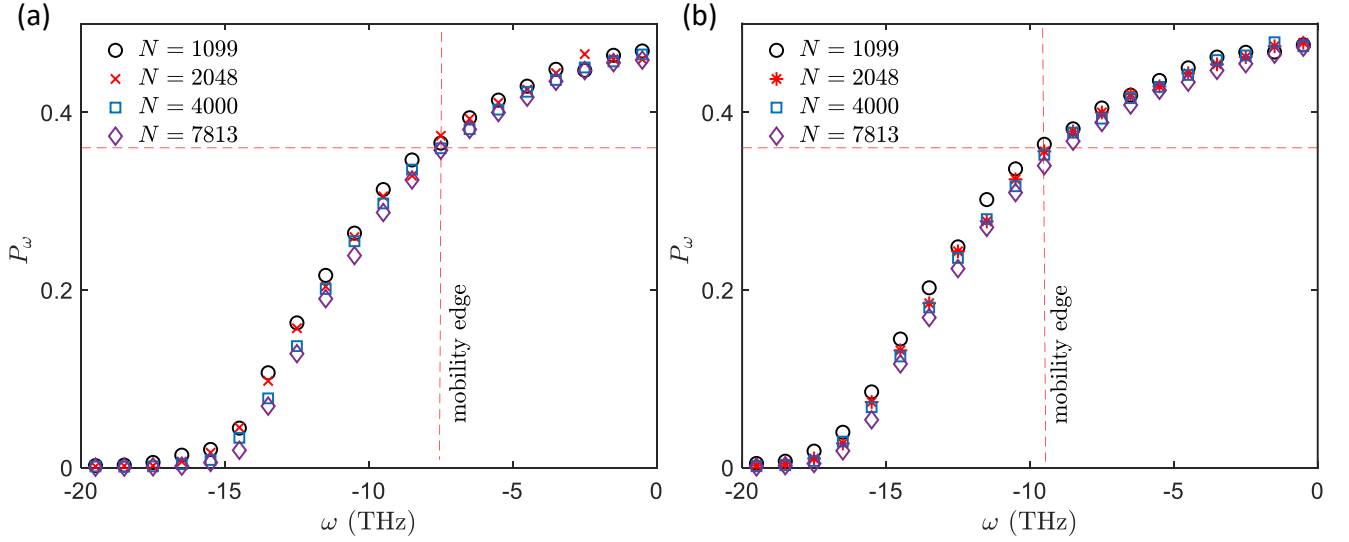


FIG. S10. Variation of the participation ratio of CuZr metallic glass-forming liquid as a function of (imaginary frequency) at (a) 1500 K and (b) 2100 K upon changing the size of the simulation box.

Appendix J: Generalized Langevin equation (GLE)

The linear generalized Langevin equation (GLE) is given by [69]

$$\dot{\mathbf{p}}(t) = -m\bar{\omega}^2\mathbf{q}(t) - \int_0^t v(t-\tau)\mathbf{v}(\tau)d\tau + \mathbf{F}_r(t), \quad (\text{S1})$$

where $\bar{\omega}$ is the frequency of an effective harmonic oscillator. Multiplying the linear GLE with $\mathbf{p}(0)$ and taking a canonical ensemble average, we can get

$$\dot{C}_{\mathbf{p}\mathbf{p}}(t) = -m\bar{\omega}^2 C_{\mathbf{p}\mathbf{q}}(t) - \int_0^t v(t-\tau)C_{\mathbf{p}\mathbf{v}}(\tau)d\tau. \quad (\text{S2})$$

By using the relation

$$C_{\mathbf{p}\mathbf{q}}(t) = \int_0^t C_{\mathbf{p}\mathbf{v}}(\tau)d\tau, \quad (\text{S3})$$

Eq. S2 can be simplified in the following form

$$\dot{C}_{\mathbf{p}\mathbf{p}}(t) = - \int_0^t K(t-\tau)C_{\mathbf{p}\mathbf{v}}(\tau)d\tau, \quad (\text{S4})$$

where

$$K(t) = v(t) + m\bar{\omega}^2. \quad (\text{S5})$$

Upon Fourier transforming Eqs. (S4) and (S5), one obtains

$$\tilde{K}(\omega) = \frac{C_{\mathbf{p}\mathbf{p}}(0)}{\tilde{C}_{\mathbf{p}\mathbf{v}}(\omega)} - i\omega, \quad (\text{S6})$$

$$\tilde{K}(\omega) = \tilde{v}(\omega) + \pi m\bar{\omega}^2\delta(\omega) - i\frac{m\bar{\omega}^2}{\omega}. \quad (\text{S7})$$

Comparing Eqs. (S6) and (S7), we finally obtain

$$\tilde{v}(0) = \lim_{\omega \rightarrow 0} \tilde{v}(\omega) \approx \lim_{\omega \rightarrow 0} \tilde{K}(\omega) = \lim_{\omega \rightarrow 0} \frac{C_{\mathbf{p}\mathbf{p}}(0)}{\tilde{C}_{\mathbf{p}\mathbf{v}}(\omega)} = \frac{C_{\mathbf{p}\mathbf{p}}(0)}{\tilde{C}_{\mathbf{p}\mathbf{v}}(\omega)} = \frac{mk_B T}{m\tilde{C}_{\mathbf{v}\mathbf{v}}(0)} = \frac{k_B T}{\int_0^\infty \langle \mathbf{v}(\mathbf{t})\mathbf{v}(\mathbf{0}) \rangle dt} = \frac{k_B T}{D}. \quad (\text{S8})$$

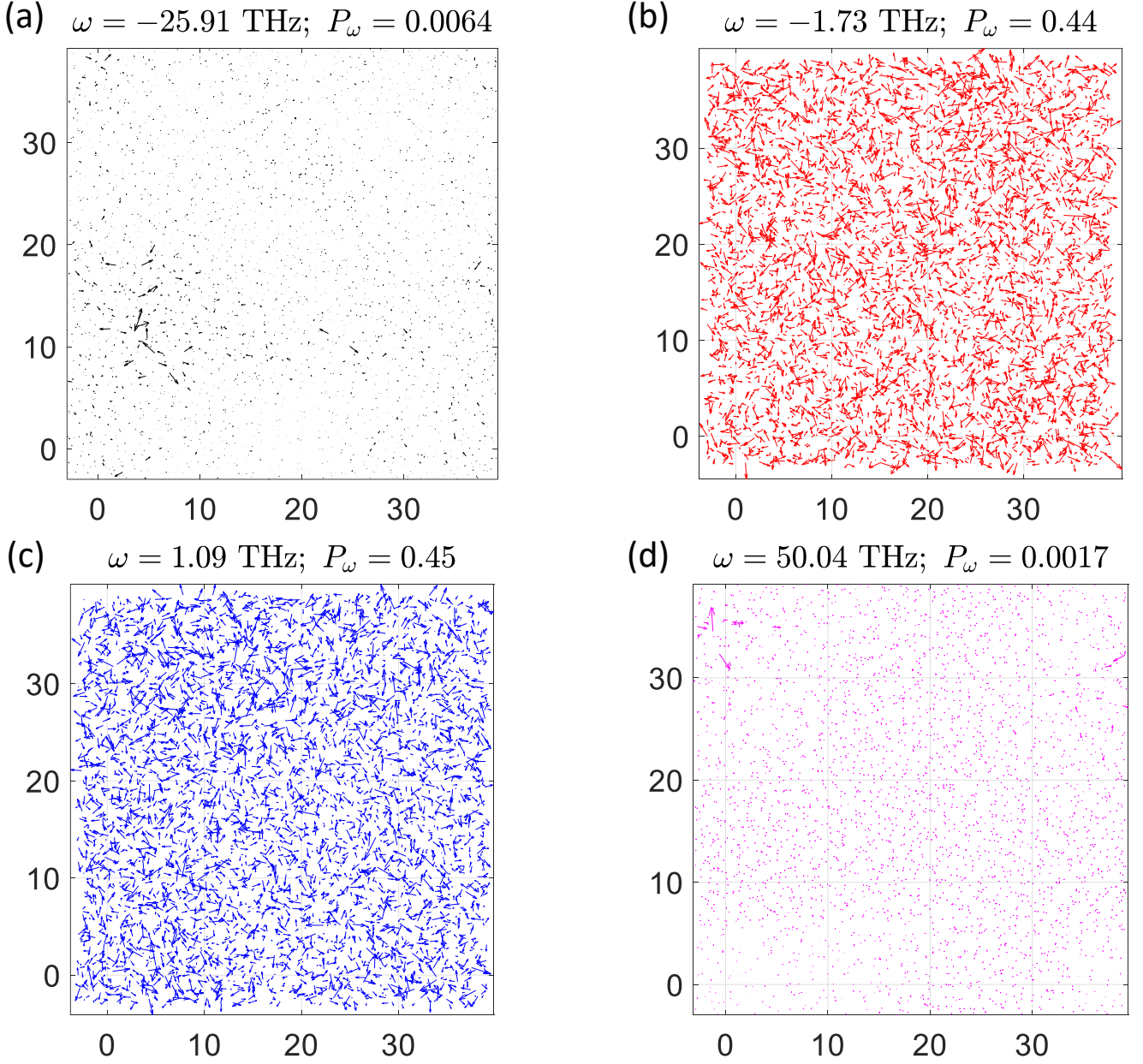


FIG. S11. Spatial projection of the eigenvectors on the xy -plane of each particle corresponding to (a) unstable localized mode ($\omega = -25.91$ THz), (b) unstable delocalized mode ($\omega = -1.73$ THz), (c) stable delocalized mode ($\omega = 1.09$ THz) and (d) stable localized mode ($\omega = 50.04$ THz) of CuZr metallic liquid at 1500 K.

Appendix K: Verification of the liquid phase

Our computations for the Cu-Zr metallic liquid extend to high temperatures, ≈ 6000 K. As evident from the results presented in the main text, the viscosity is perfectly captured by the ULINM even at high temperatures. Here, we show that, despite the large temperatures, the Cu-Zr metallic liquid is still in the liquid state. This is explicitly proven by both the pair distribution function $g(r)$ and the velocity autocorrelation function VACF shown in Fig. S14. As evident from there, below 6000 K the system has still liquid characteristics.

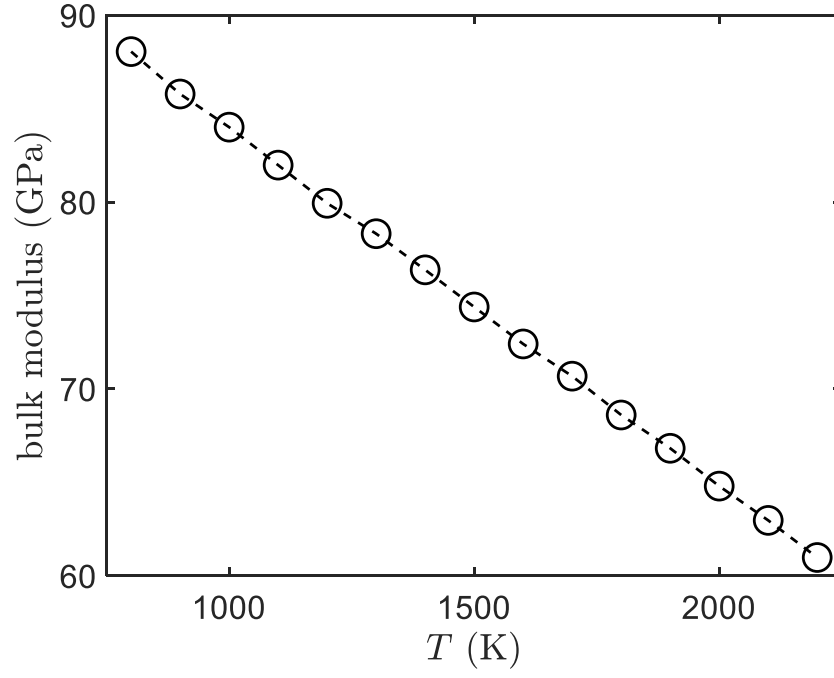


FIG. S12. Temperature dependence of bulk modulus for the CuZr metallic glass-forming system.

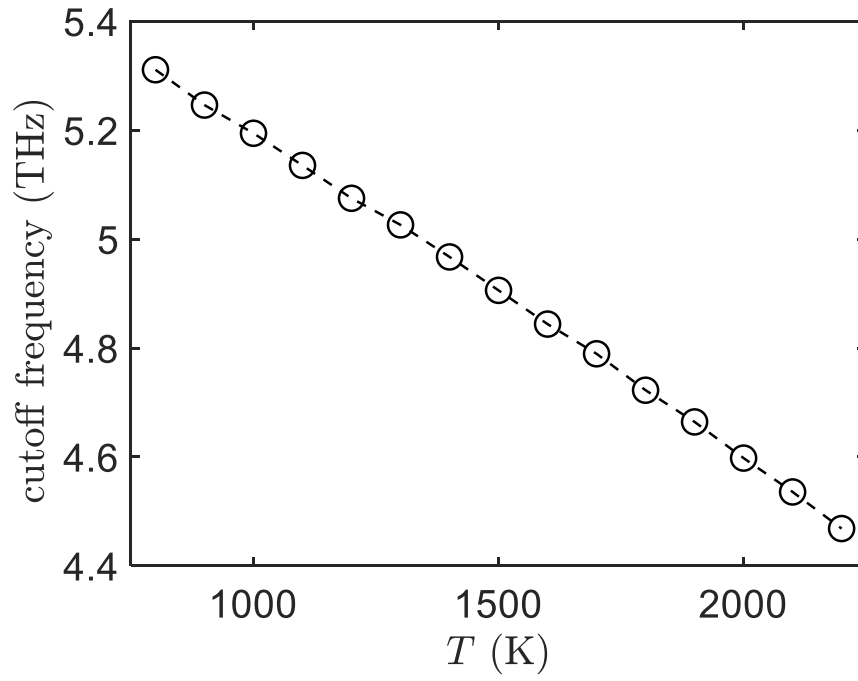


FIG. S13. Temperature dependence of cutoff frequency ω_{\min} for the CuZr metallic glass-forming system.

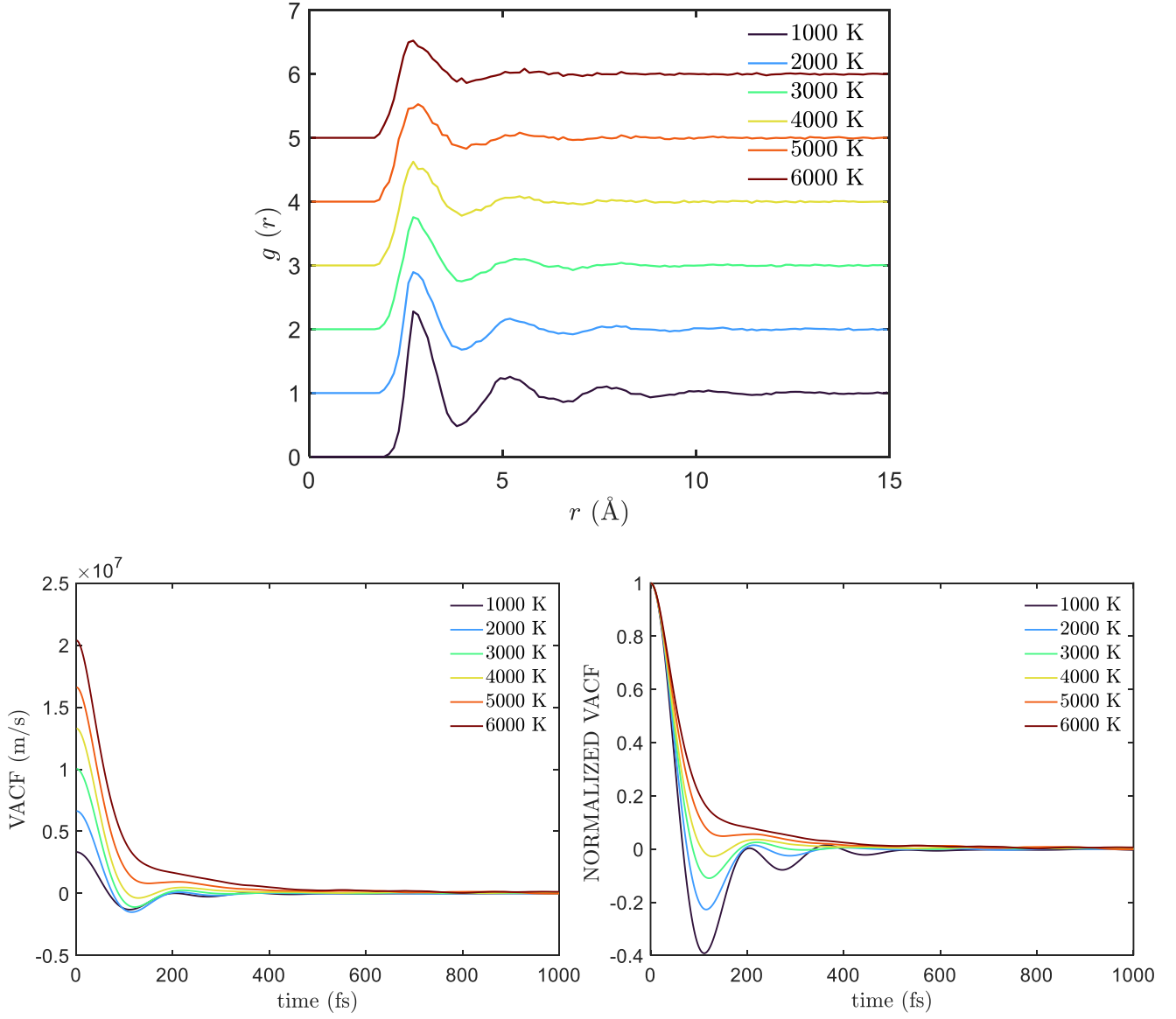


FIG. S14. **Top panel:** pair distribution function $g(r)$ for the Cu-Zr metallic liquid at different temperatures. **Bottom panel:** velocity auto-correlation function VACF for the same system.